ADVANCED ENERGY MATERIALS

Supporting Information

for *Adv. Energy Mater.*, DOI 10.1002/aenm.202304074

Unlocking Electrode Performance of Disordered Rocksalt Oxides Through Structural Defect Engineering and Surface Stabilization with Concentrated Electrolyte

*Yanjia Zhang, Yosuke Ugata, BenoîtDenis Louis Campéon and Naoaki Yabuuchi**

Supporting Information

Unlocking Electrode Performance of Disordered Rocksalt Oxides Through Structural Defect Engineering and Surface Stabilization with Concentrated Electrolyte

Yanjia Zhang, Yosuke Ugata, Benoît Denis Louis Campéon, and Naoaki Yabuuchi*

Dr. Y. Zhang, Dr. Y. Ugata, Dr. Benoît D.L. Campéon, and Prof. N. Yabuuchi
Advanced Chemical Energy Research Center, Institute of Advanced Sciences, Yokohama National University
Yokohama, Kanagawa 240-8501, Japan
E-mail: yabuuchi-naoaki-pw@ynu.ac.jp

Dr. Y. Ugata and Prof. N. Yabuuchi
Department of Chemistry and Life Science,
Yokohama National University
Yokohama, Kanagawa 240-8501, Japan

Dr. Benoît D.L. Campéon
University Grenoble Alpes, University Savoie Mont Blanc, CNRS, Grenoble INP, LEPMI, Grenoble, France

*Corresponding author
E-mail: yabuuchi-naoaki-pw@ynu.ac.jp

Supporting Figures

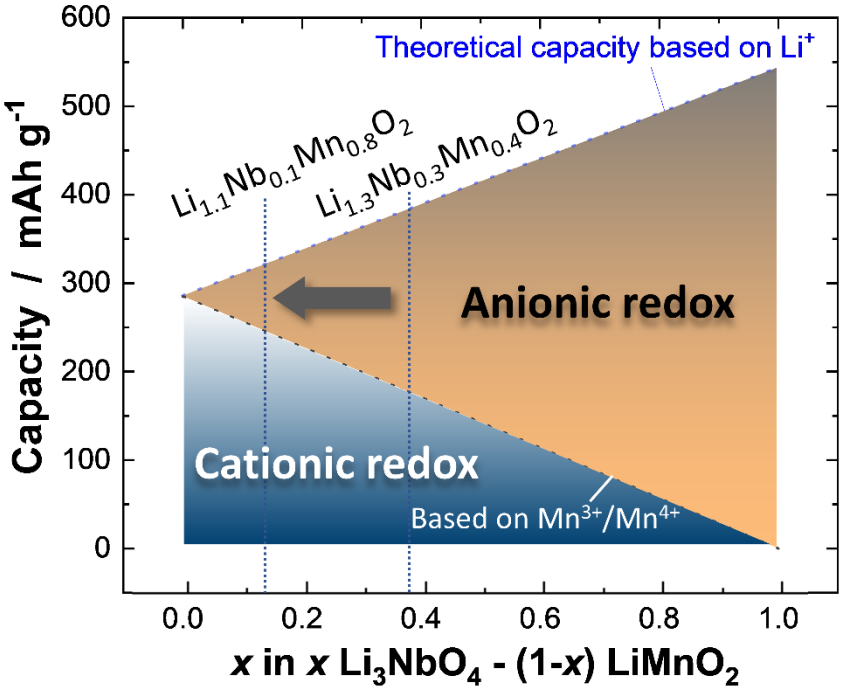

Figure S1. Theoretical capacities of Li_3NbO_4–$LiMnO_2$ binary systems with different chemical compositions. Theoretical capacities estimated based on the cationic (Mn^{3+}/Mn^{4+} redox) and anionic (O^{2-}/O^{n-} redox) are also shown.

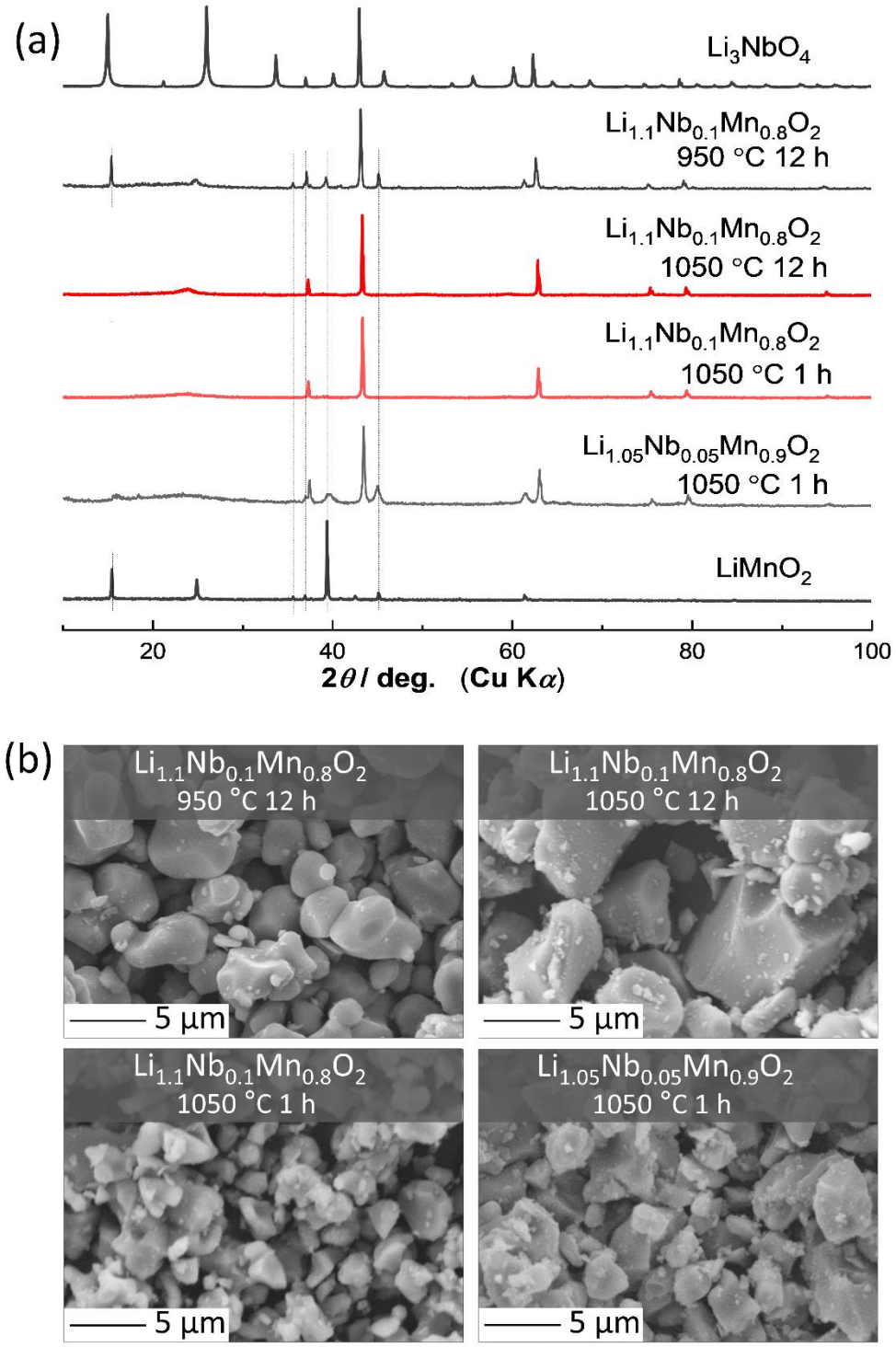

Figure S2. (a) XRD patterns and (b) SEM images of $Li_{1.1}Nb_{0.1}Mn_{0.8}O_2$ and $Li_{1.05}Nb_{0.05}Mn_{0.9}O_2$ synthesized at different temperature and time. The data of Li_3NbO_4 and $LiMnO_2$ are also shown for comparison. A pure phase of $Li_{1.05}Nb_{0.05}Mn_{0.9}O_2$ cannot be obtained.

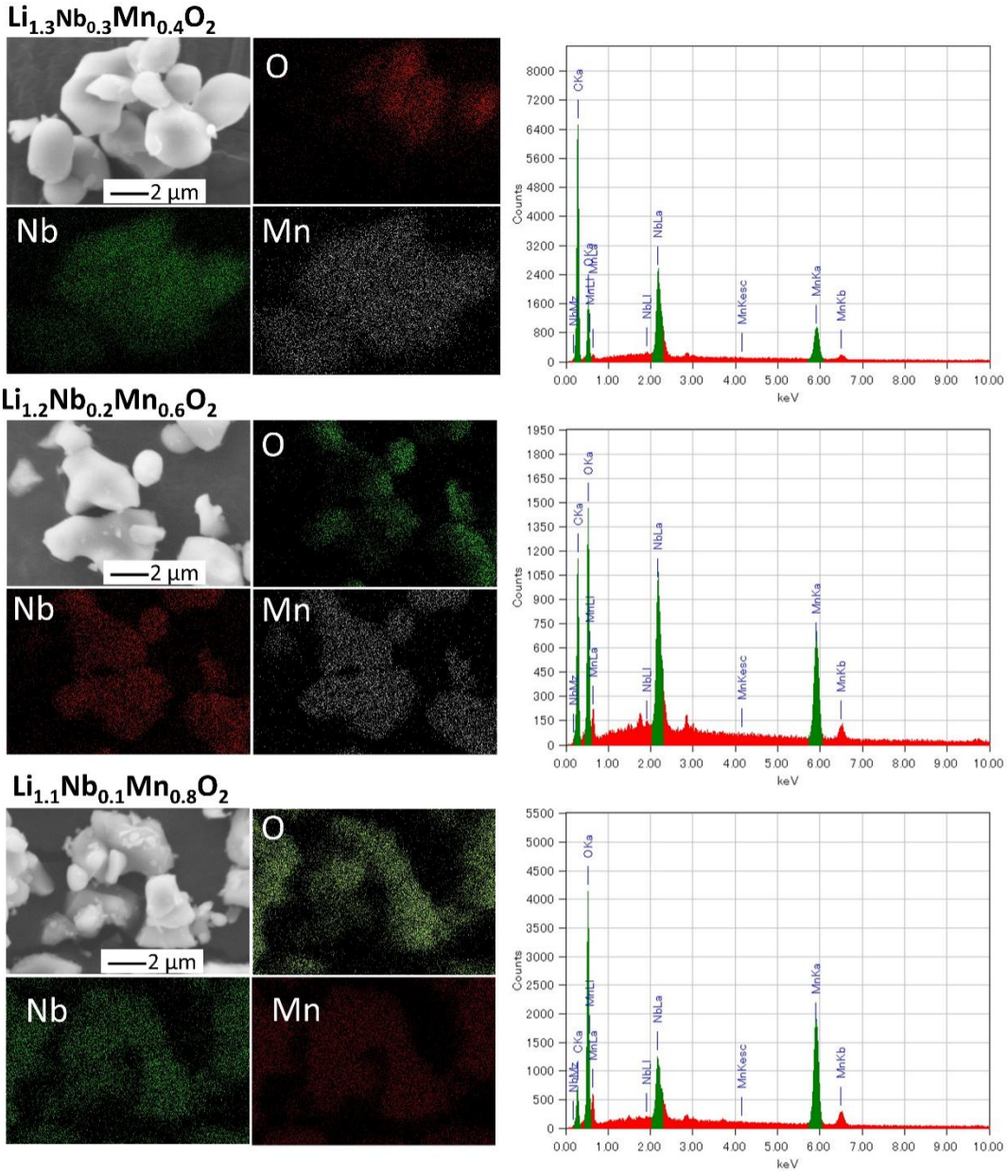

Figure S3. SEM images with EDX analysis of $Li_{1.3}Nb_{0.3}Mn_{0.4}O_2$, $Li_{1.2}Nb_{0.2}Mn_{0.6}O_2$, and $Li_{1.1}Nb_{0.1}Mn_{0.8}O_2$.

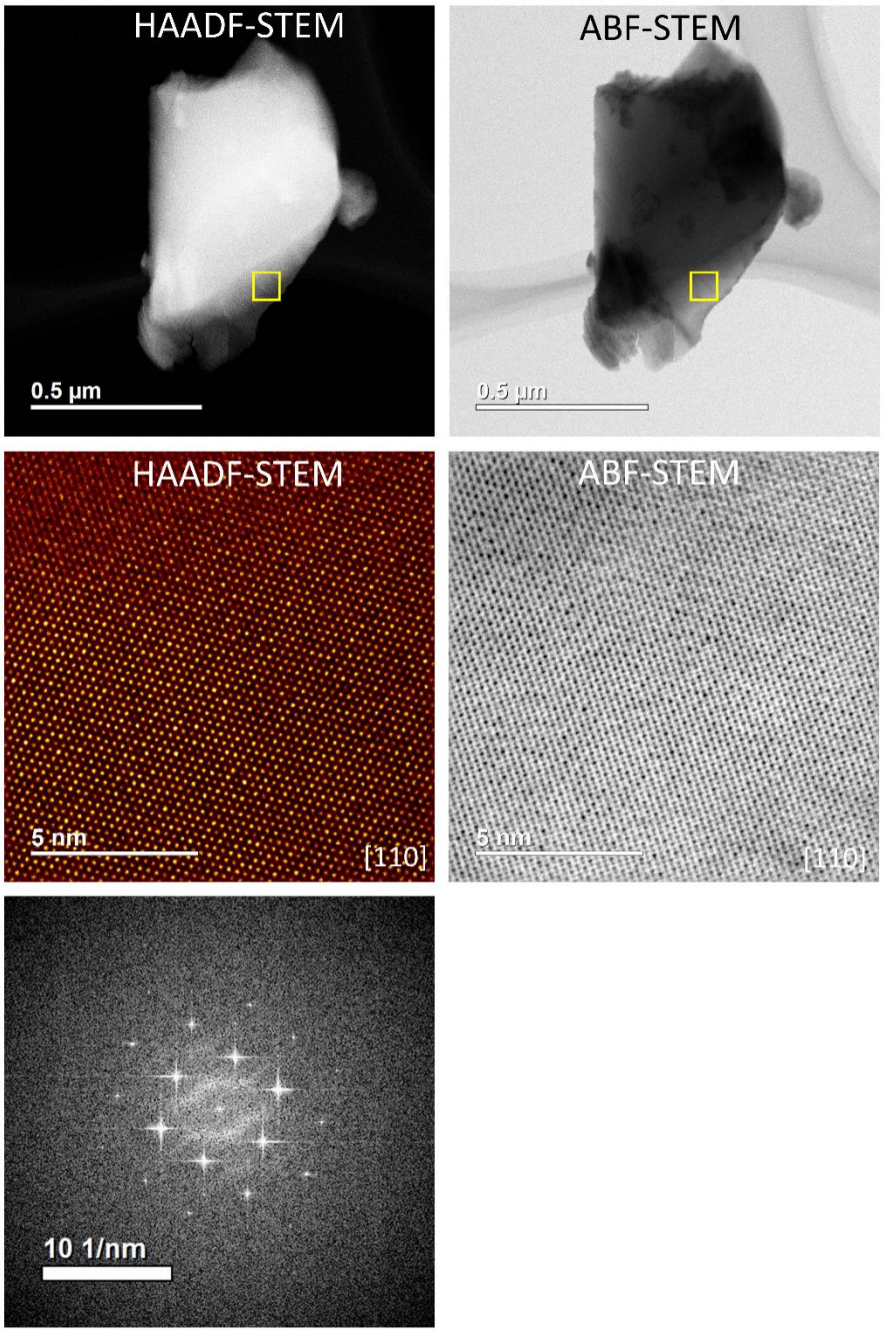

Figure S4. HAADF-/ABF-STEM images of $Li_{1.1}Nb_{0.1}Mn_{0.8}O_2$ along [011], and high magnification images are shown in **Figure 1c**. An FFT image is obtained in the yellow square area, and some diffuse spots, which are indicative of short-range cation ordering, are observed (also see **Figure 1e** and **Supporting Figure S5**).

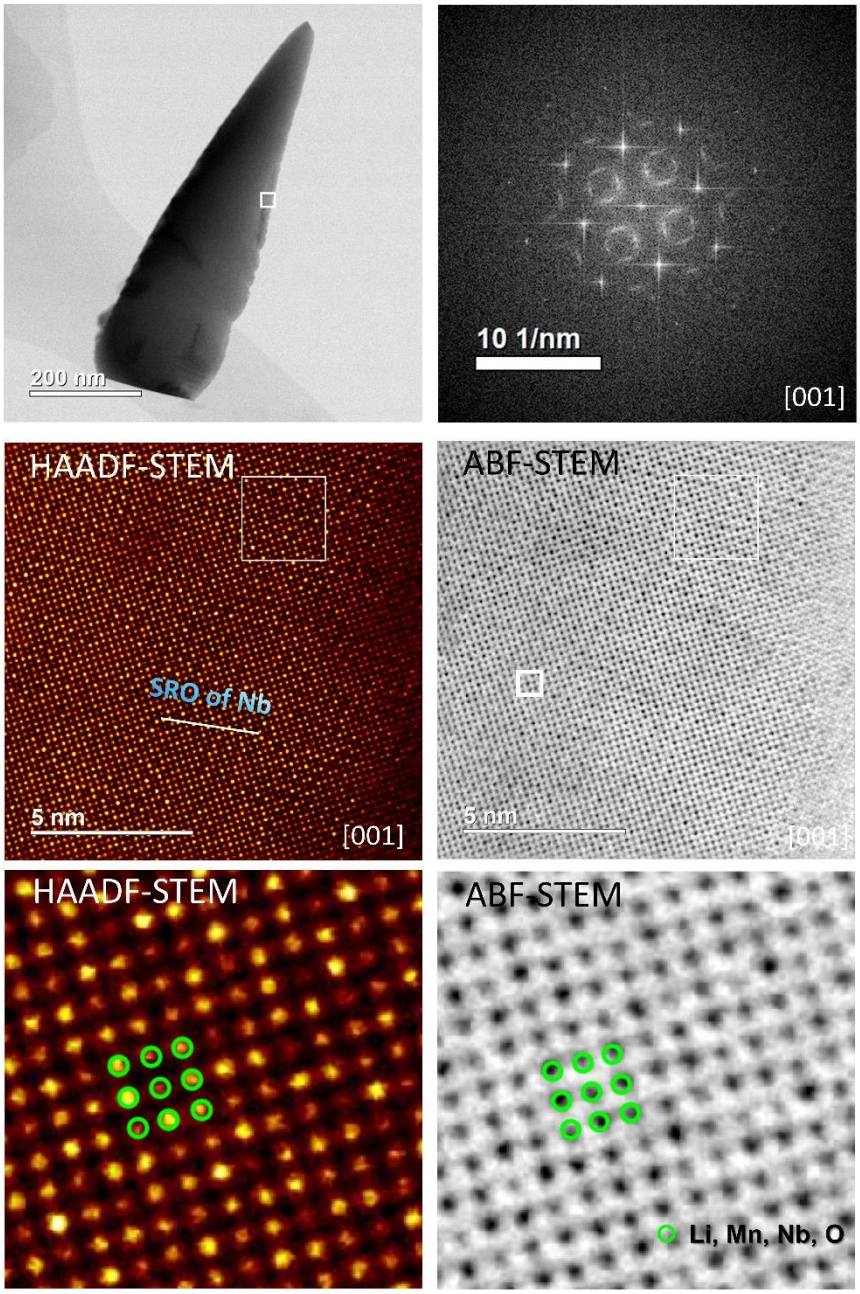

Figure S5. HAADF/ABF-STEM images of $Li_{1.1}Nb_{0.1}Mn_{0.8}O_2$ along [001] and an FFT image in the white square area in the low magnification image. Li, Nb, Mn, and O ions are randomly scattered along [001] zone axis, and the clear evidence of SRO is observed in the STEM image along [001].

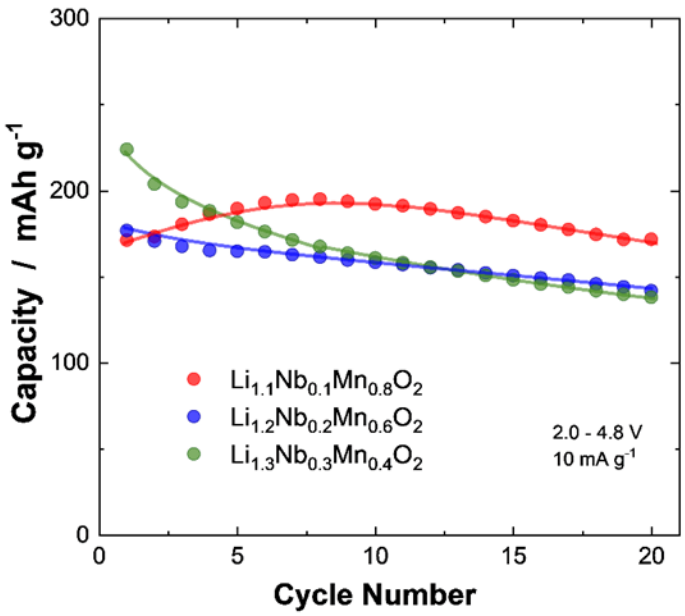

Figure S6. Cycle performance of $Li_{1.3}Nb_{0.3}Mn_{0.4}O_2$, $Li_{1.2}Nb_{0.2}Mn_{0.6}O_2$, and $Li_{1.1}Nb_{0.1}Mn_{0.8}O_2$ with a voltage range of 2.0 – 4.8 V at 10 mA g^{-1}.

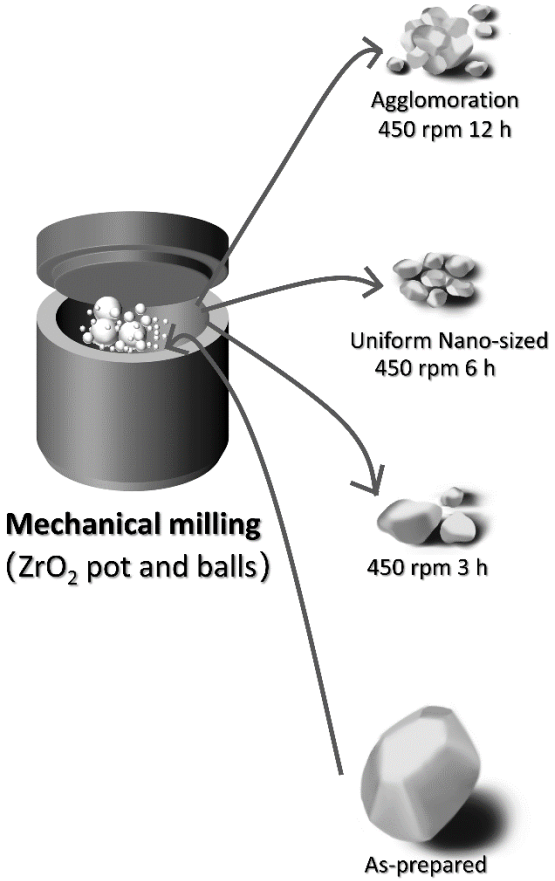

Figure S7. A schematic illustration of the synthesis of nanosized samples by mechanical milling.

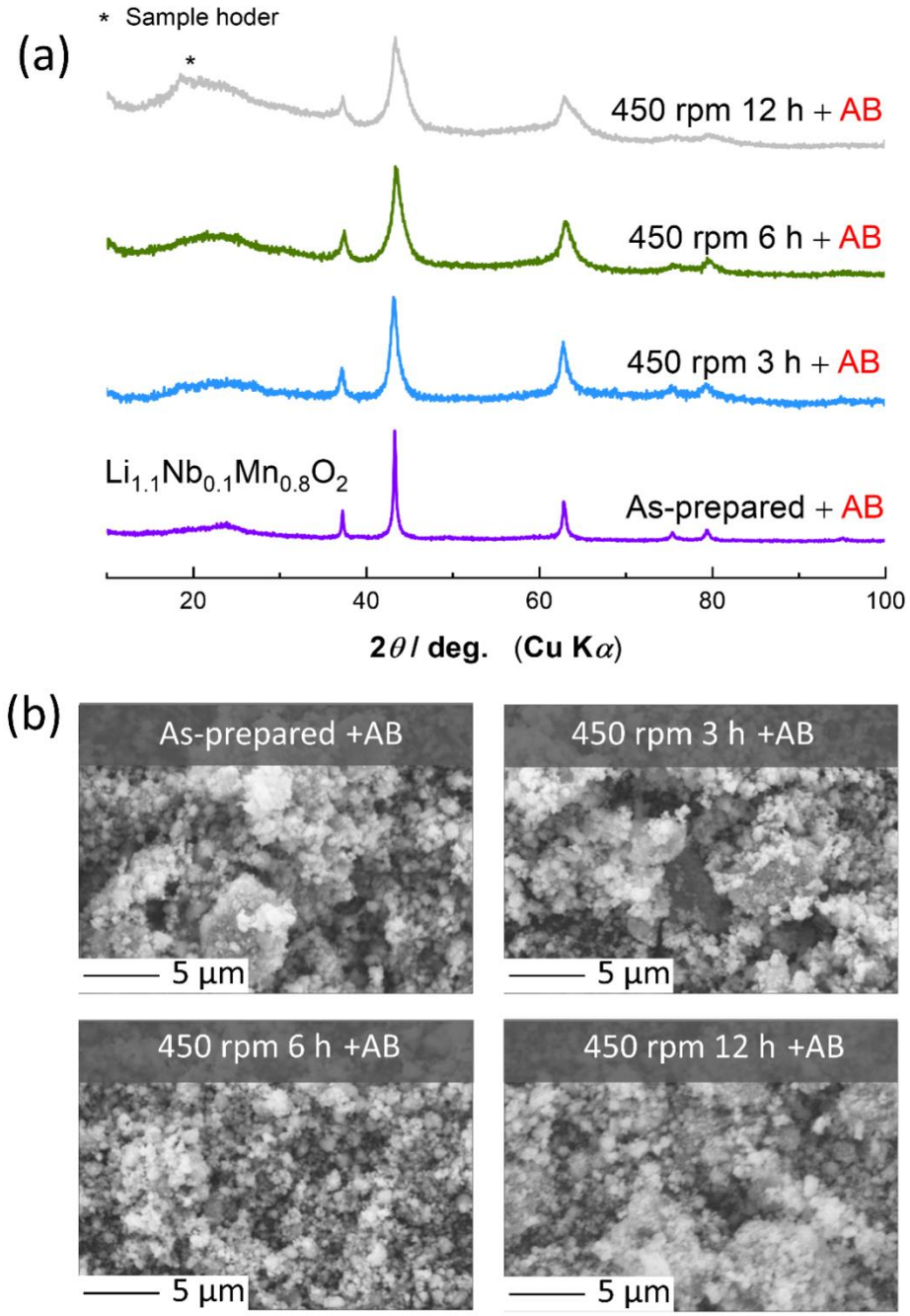

Figure S8. (a) XRD patterns and (b) SEM images of as-prepared $Li_{1.1}Nb_{0.1}Mn_{0.8}O_2$ samples milled at 450 rpm for 3 h, 6 h, and 12 h, after mixing with acetylene black.

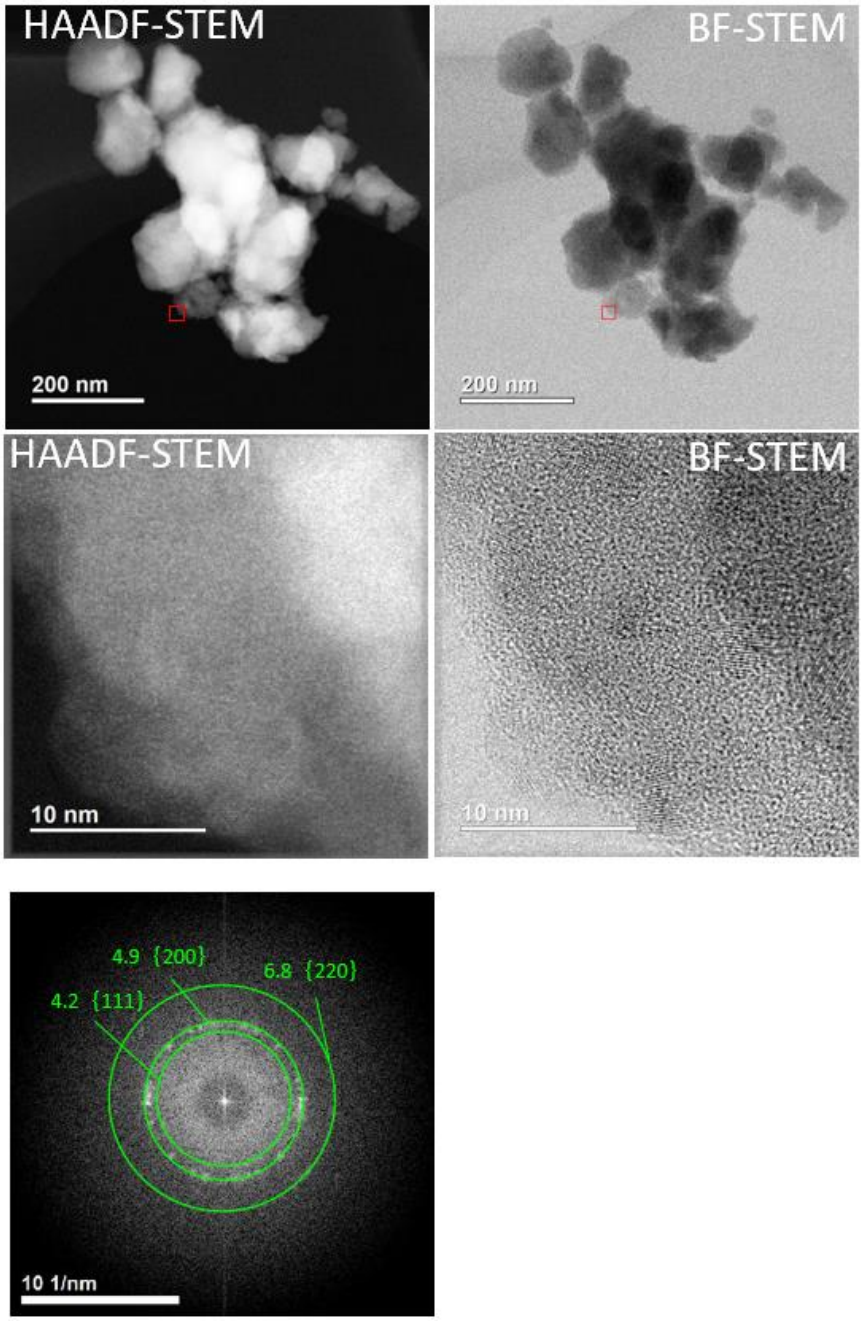

Figure S9. HAADF/ABF-STEM images of nanosized $Li_{1.1}Nb_{0.1}Mn_{0.8}O_2$, 450 rpm 6 h milled sample, with different magnifications. An FFT image of STEM image is also shown.

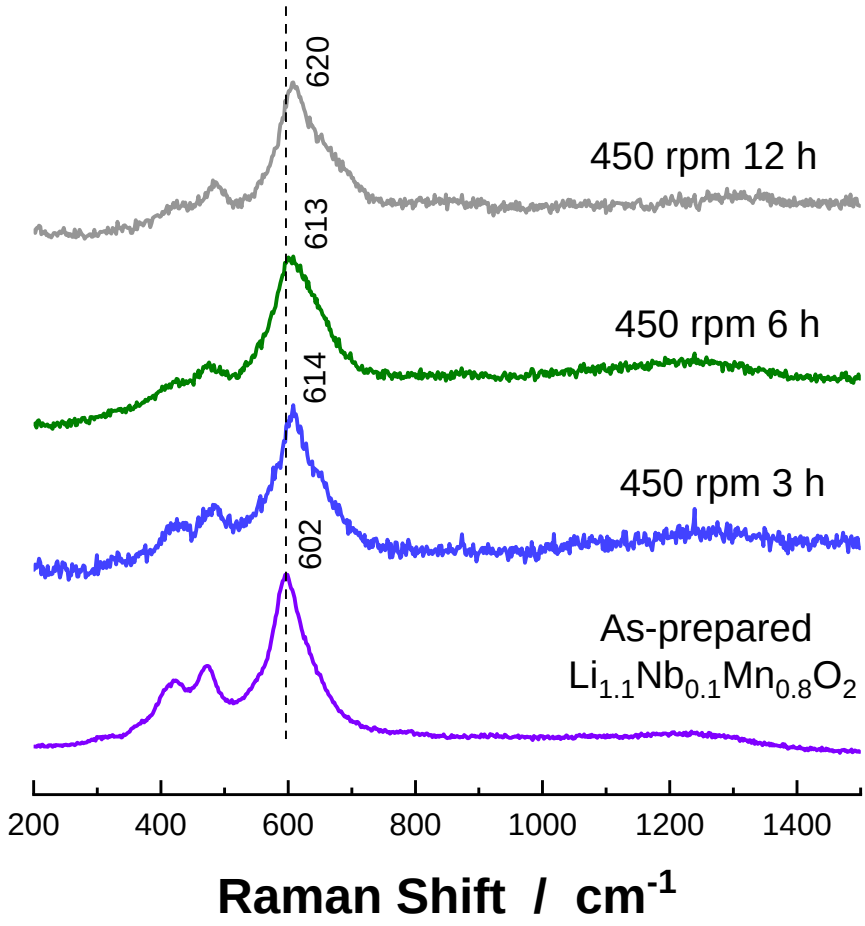

Figure S10. Raman spectra of as-prepared, 450 rpm 3 h, 6 h, and 12 h milled samples.

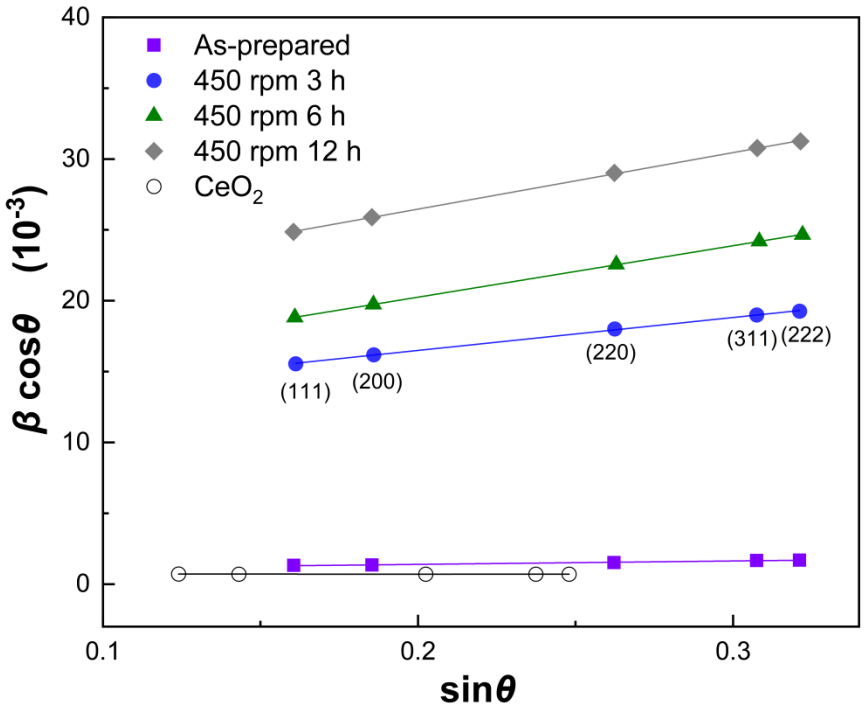

Figure S11. Williamson–Hall plots of the different samples: as-prepared, 450 rpm 3h, 6 h, and 12 h. A CeO_2 standard was also analyzed for instrumental calibration.

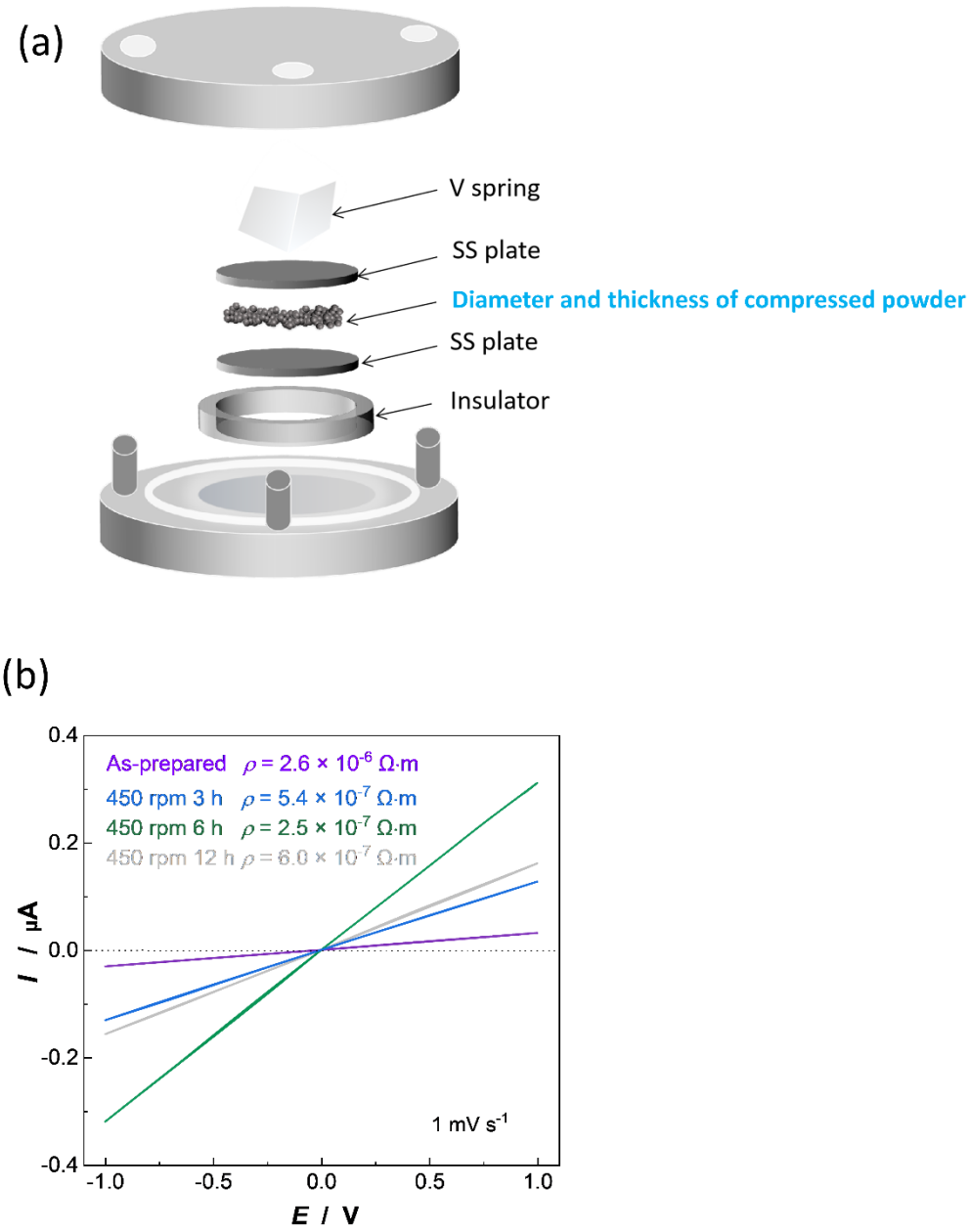

Figure S12. (a) A scheme of the experimental setup of electronic conductivity measurement for powder samples, and (b) reproduced data obtained from different powders synthesized at the same condition in **Figure 3c**.

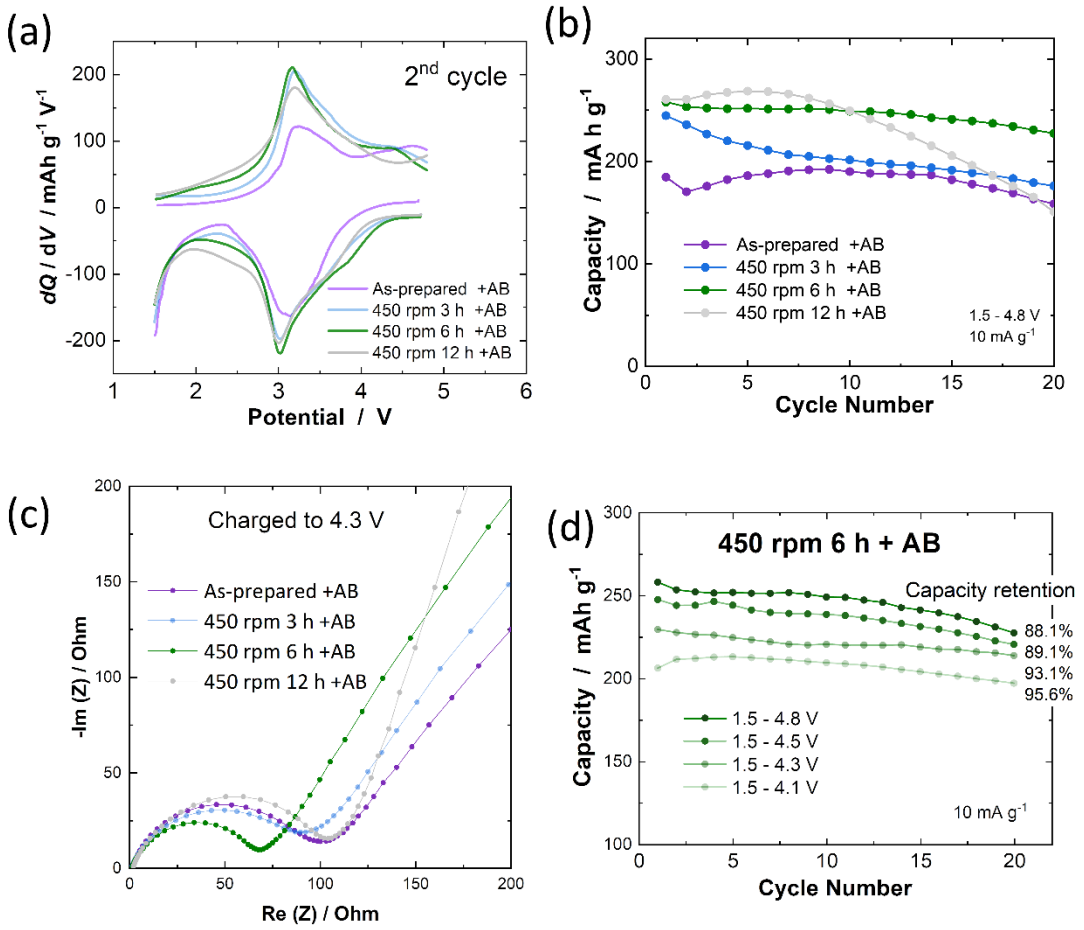

Figure S13. Comparison of electrode performance before and after mechanical milling with different duration: (a) differential capacity curves, (b) cycle stability, (c) EIS spectra after charged to 4.3 V, and (d) cycle performance of 450 rpm 6 h milled $Li_{1.1}Nb_{0.1}Mn_{0.8}O_2$ at different cut-off voltages.

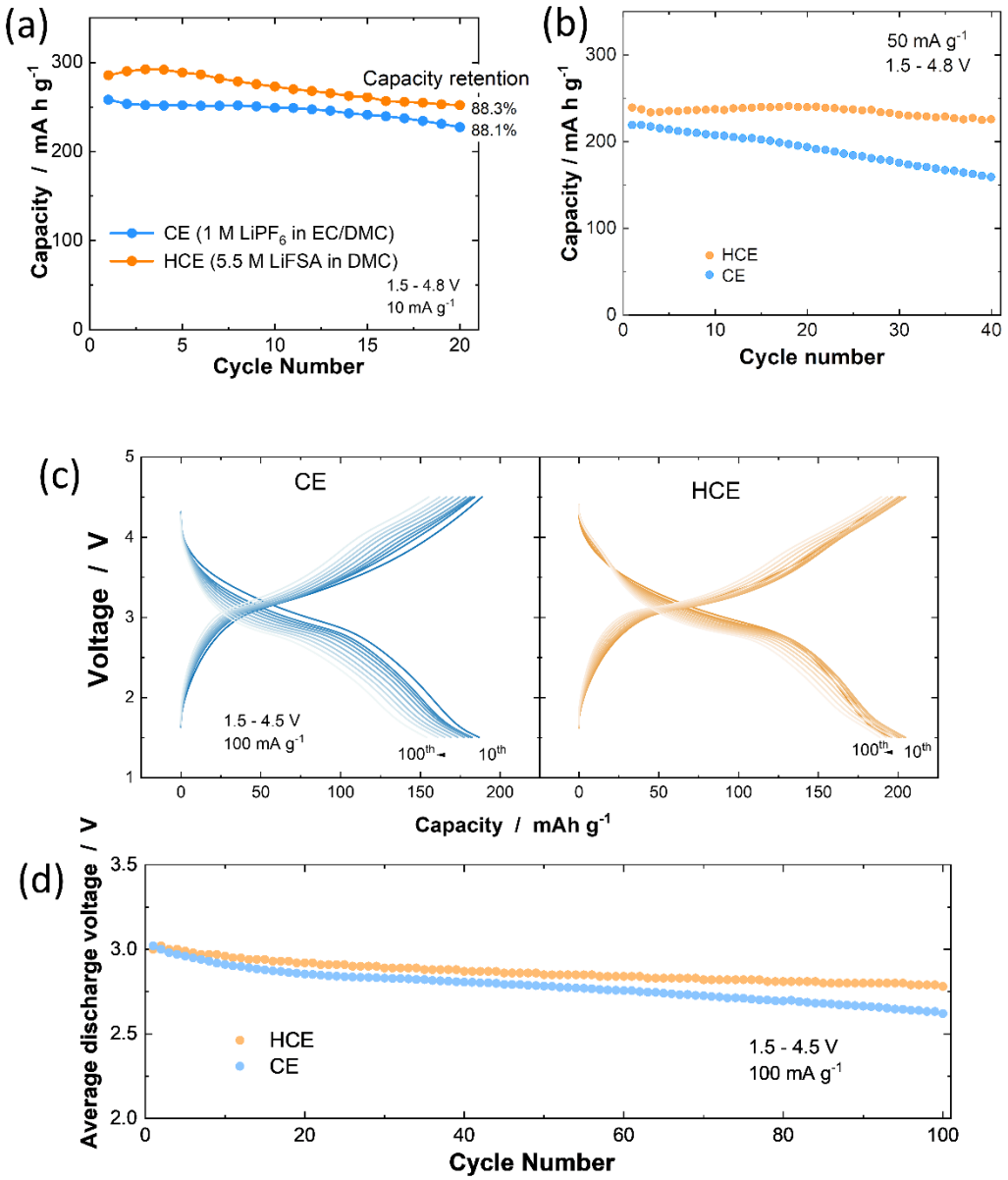

Figure S14. Electrode performance of nanosized $Li_{1.1}Nb_{0.1}Mn_{0.8}O_2$, 450 rpm 6 h milled sample, cycled in CE and HCE: cyclability at a rate of (a) 10 mA g^{-1} and (b) 50 mA g^{-1} with the voltage range of 1.5–4.8 V. (c) Galvanostatic charge/discharge curves cycling in CE and HCE at 100 mA g^{-1} with voltage range of 1.5–4.5 V and (d) average discharge voltage variations for 100 cycles.

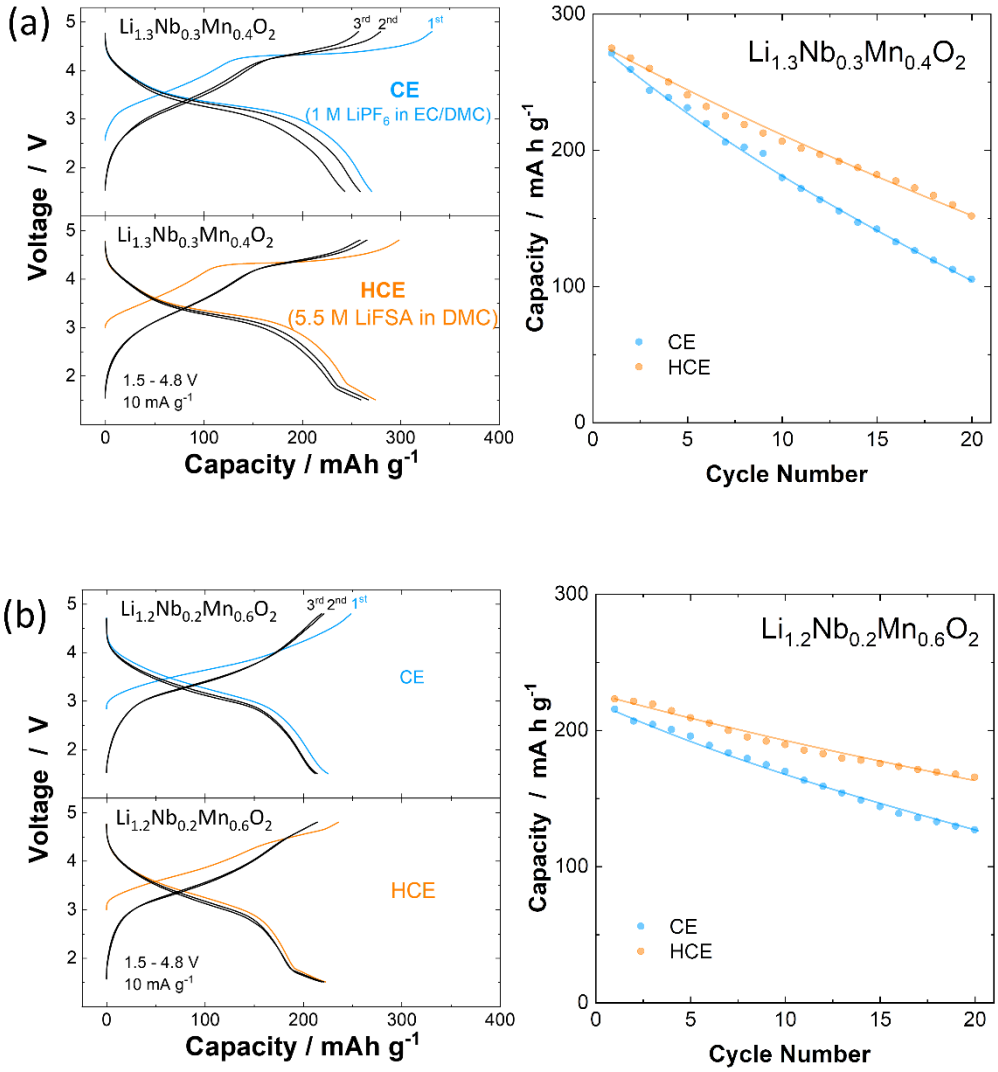

Figure S15. Electrode performance comparison of micrometer-sized (a) $Li_{1.3}Nb_{0.3}Mn_{0.4}O_2$ and (b) $Li_{1.2}Nb_{0.2}Mn_{0.6}O_2$ cycled in CE and HCE.

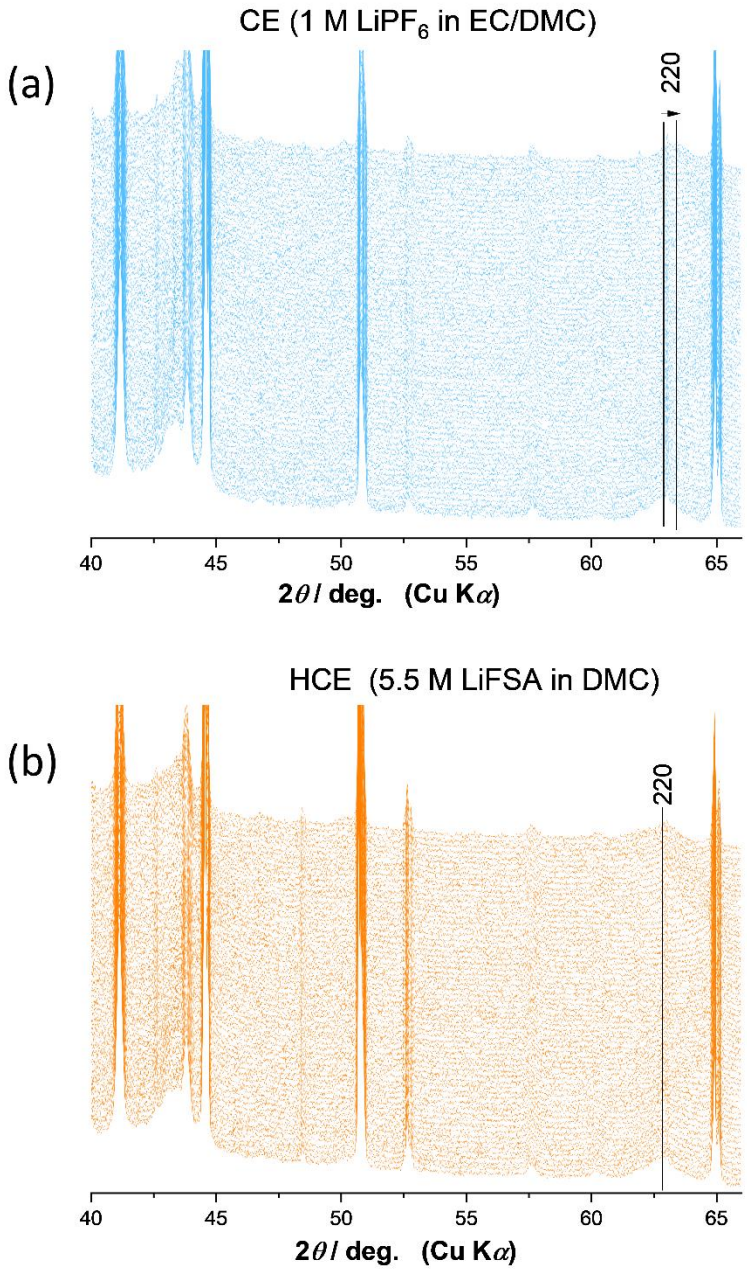

Figure S16. Original in-situ XRD data of nanosized $Li_{1.1}Nb_{0.1}Mn_{0.8}O_2$ cycled in (a) CE and (b) HCE. Many diffraction peaks originate from Be window and Al current collector.

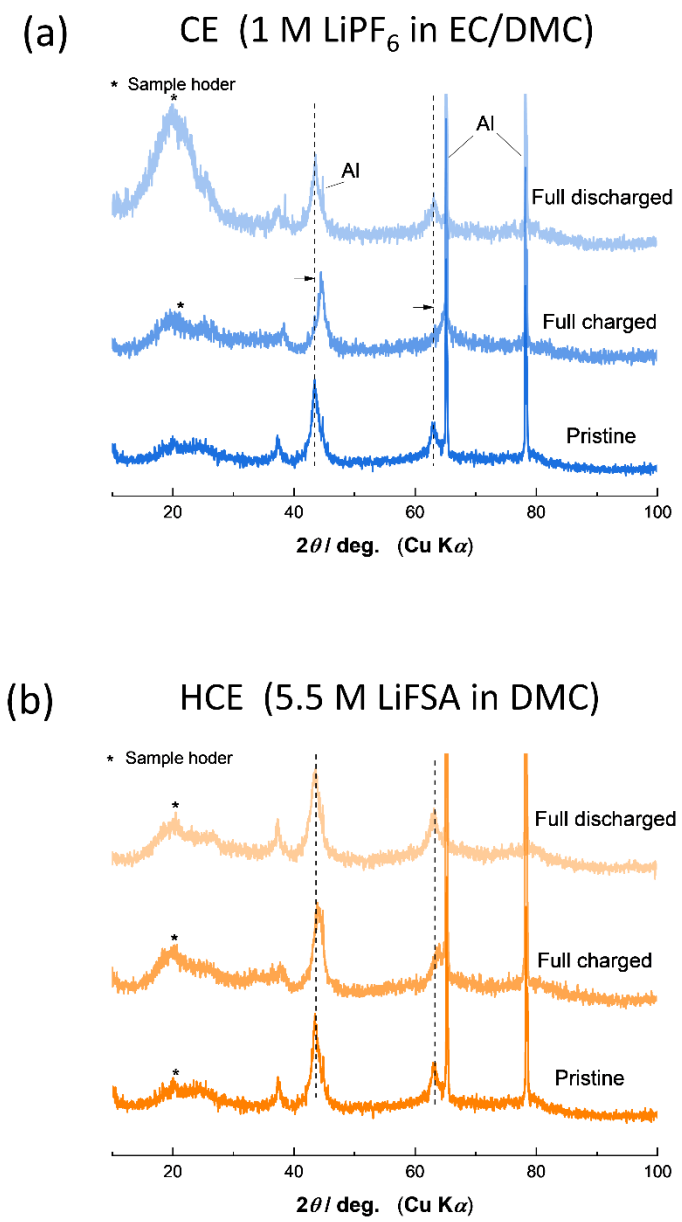

Figure S17. Ex-situ XRD data of nanosized $Li_{1.1}Nb_{0.1}Mn_{0.8}O_2$ cycled in (a) CE and (b) HCE.

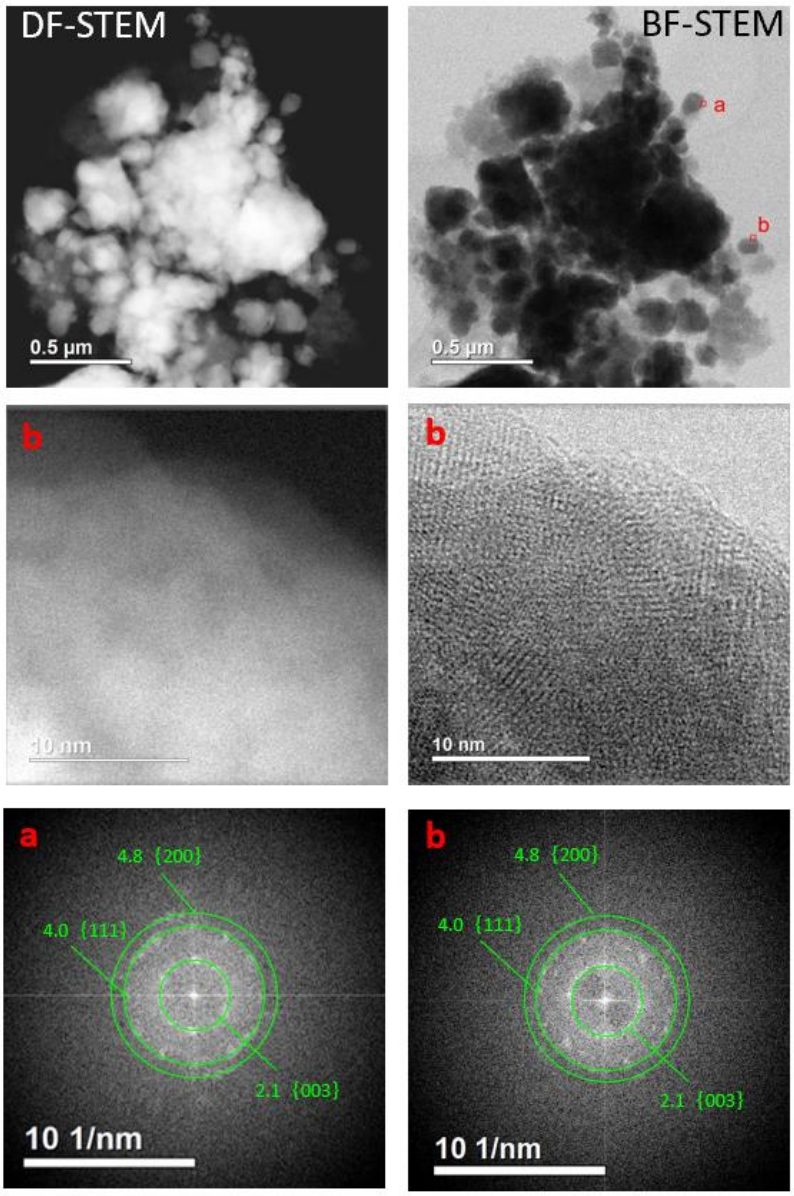

Figure S18. DF/BF-STEM and FFT images of nanosized $Li_{1.1}Nb_{0.1}Mn_{0.8}O_2$ cycled in HCE with different magnifications. The red square "a" is the location for STEM images shown in **Figure 6b**.

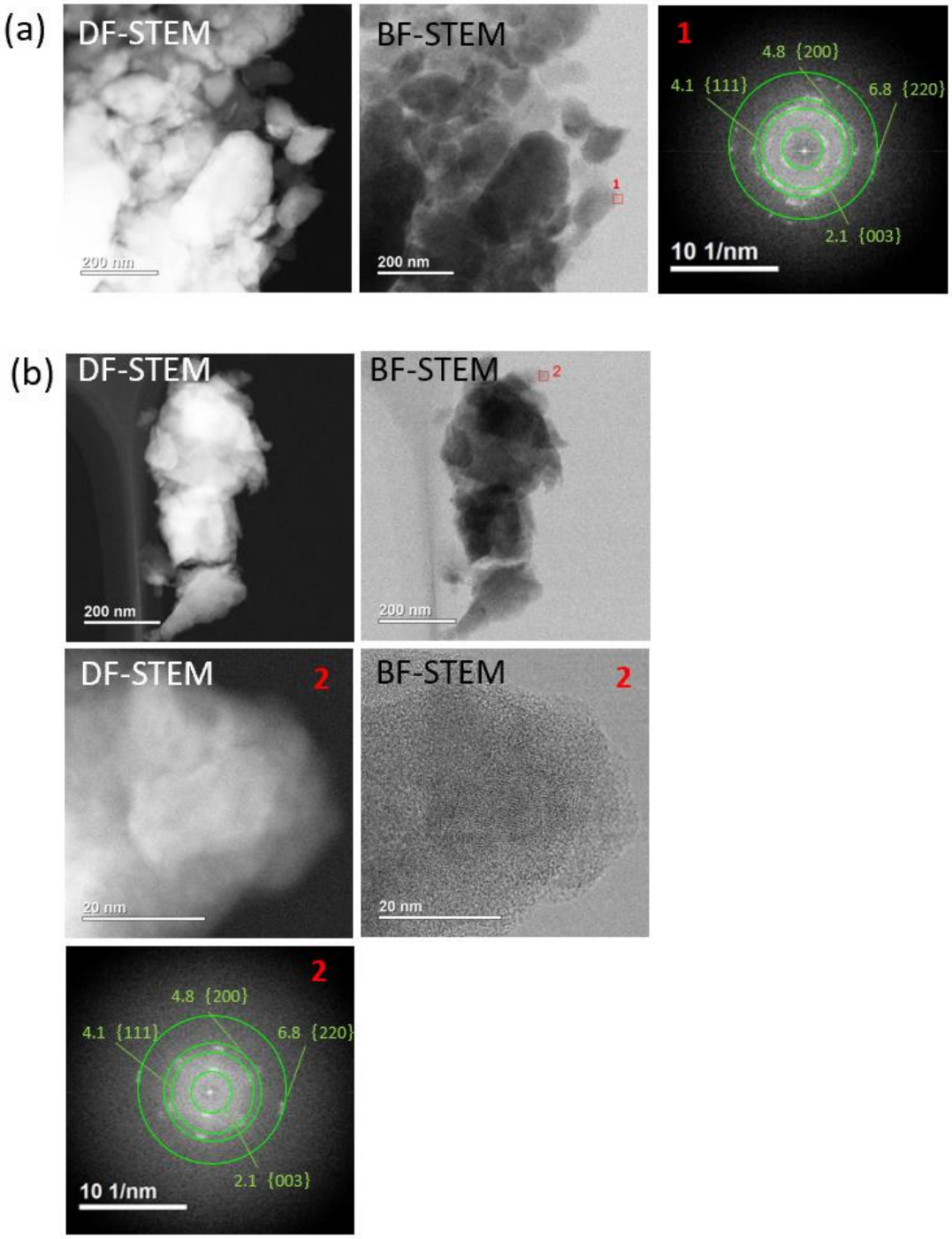

Figure S19. DF/BF-STEM and FFT images of (a) nanosized $Li_{1.1}Nb_{0.1}Mn_{0.8}O_2$ cycled in CE, the red square "1" is the location for STEM images shown in **Figure 6b**, and (b) the sample measured from a different particle.

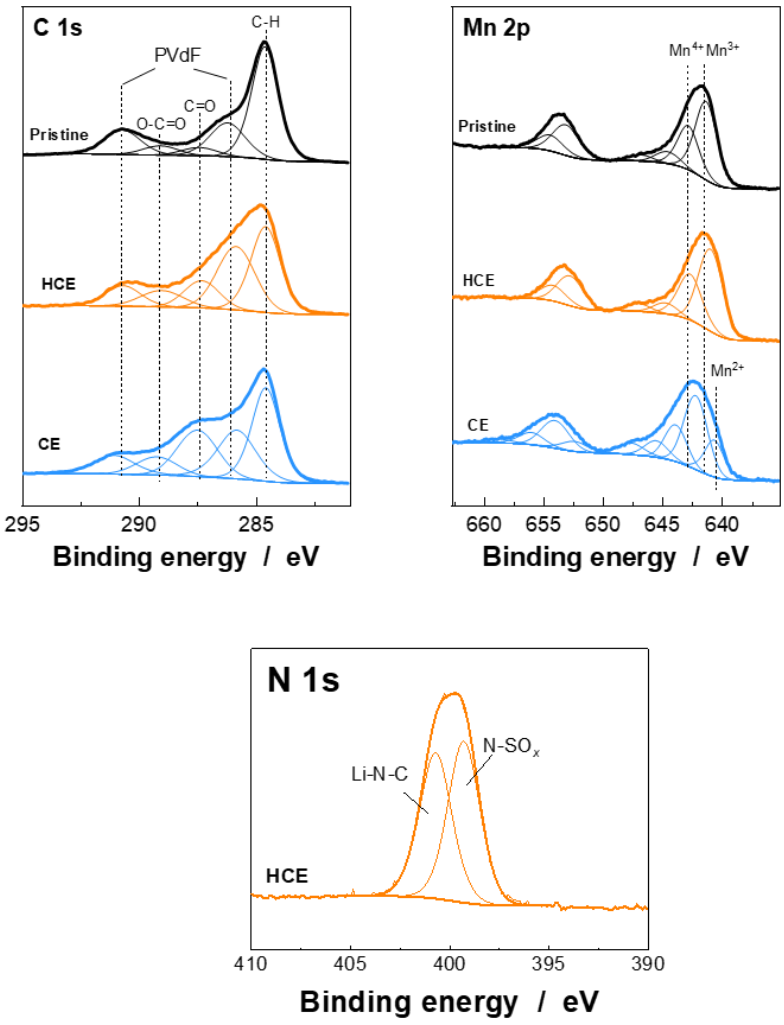

Figure S20. XPS spectra of nanosized $Li_{1.1}Nb_{0.1}Mn_{0.8}O_2$ before and after cycle in HCE and CE: C 1s, Mn 2p, and N 1s XPS spectra.